

1 **Diversity of soluble salt concentrations on volcanic ash aggregates from a variety of**
2 **eruption types and deposits**

3 Mathieu Colombier¹; Sebastian B. Mueller², Ulrich Kueppers¹, Bettina Scheu¹, Pierre
4 Delmelle³, Corrado Cimarelli¹, Shane J. Cronin⁴, Richard J. Brown⁵, Manuela Tost⁴, and
5 Donald B. Dingwell¹

6
7 ¹Department of Earth and Environmental Sciences, Ludwig-Maximilians-Universität
8 München, Germany; ²Department of Geology and Geophysics, University of Hawaii at Mānoa,
9 Honolulu, Hawaii, USA; ³Université catholique de Louvain, Earth & Life Institute,
10 Environmental Sciences, Belgium; ⁴School of Environment, University of Auckland, New
11 Zealand; ⁵Department of Earth Sciences, Durham University, UK

12

13 **Keywords**

14 **Ash aggregates**, leaching, salt precipitation, particle binding, **plume dispersal**

15

16 **Abstract**

17 Ash aggregation is a common phenomenon in particle-laden environments of volcanic eruption
18 plumes and pyroclastic density currents. Many of these initially fragile aggregates gain
19 sufficient mechanical strength to remain intact after atmospheric transport and deposition.
20 Several processes contribute to ash aggregate stability, including: electrostatic and hydrostatic
21 bonding, ice formation and cementation by salt precipitates. Here, we compare leachate
22 chemistry from aggregates from a variety of eruption and sedimentation conditions, ranging
23 from dry magmatic eruptions with immediate deposition, to eruptions through seawater. The
24 leachate data shows that the broad window of opportunity for aggregation and aggregate
25 breakup may be used to qualitatively constrain suspended ash concentration and its temporal
26 evolution. We show that aggregation rate and aggregate stability largely depend on the
27 availability of external water and salt source. In particular, high humidity and extensive salt
28 precipitation in seawater environments, such as **during** Surtseyan eruptions, promote high
29 aggregation rates and aggregate stability, with accordingly accentuated proximal deposition and
30 aggregate concentration in the deposits. On the other hand, low humidity and salt concentrations
31 during dry magmatic eruptions promote **less** aggregation and more efficient aggregate break-
32 up, explaining the rarity of aggregates in the deposits. These results have strong implications

33 for the ash budget in volcanic plumes and associated models of plume dispersal and related
34 hazards.

35

36 **Introduction**

37 Ash aggregation is a common phenomenon associated with explosive volcanism. Volcanic ash
38 particles in both eruptive plumes and pyroclastic density currents (PDCs) are believed to
39 experience repeated contact with other particles (Saxby et al. 2018; Costa et al. 2006; Draxler
40 and Hess 1997). Upon approach and contact, the physical forces of electrostatic or hydrostatic
41 bonding (Alois et al. 2017; Mueller et al. 2016; Del Bello et al. 2015; Van Eaton et al. 2012;
42 Costa et al. 2010; James et al. 2002; Gilbert and Lane 1994) may help to overcome rebounding
43 forces and thereby enhance aggregate growth (Ennis et al. 1991). Only aggregates strong
44 enough to survive atmospheric transport and deposition are preserved in the geological record.
45 These can be used as conservative input parameter for residence time of suspended ash
46 influencing ash dispersal (Folch et al. 2010). The adhesion forces of hydrostatic bonding (that
47 is related to hydrogen bonding due to polarity of H₂O molecules) and electrostatic bonding are
48 too weak for long-term aggregation ($<10^4$ nN, Salman et al. 2006), so that other mechanisms
49 must stabilize new aggregates during transport and deposition. One key stabilization process is
50 the precipitation of soluble salts in inter-particle voids (Mueller et al. 2016).

51 **Several** studies (e.g., Gilbert and Lane 1994; Kueppers et al. 2016) demonstrated the
52 presence of salts in aggregates, **and** their importance in stabilizing aggregates has been
53 demonstrated both experimentally and numerically (Mueller et al. 2017a, b). Both volcanic and
54 environmental gases and fluids can drive salt precipitation on volcanic ash surfaces. Ayris et al.
55 (2013, 2014) showed how the direct adsorption of volcanic gases such as SO₂, HCl or HF drive
56 diffusion-driven salt precipitation. Also, salts form by condensation of acidic liquid droplets (or
57 aerosols) on ash surfaces (Rose 1977; Hoshyaripour et al. 2014). During transport in volcanic
58 plumes, ash particles may become partially- or fully-coated with aerosol droplets (Delmelle et
59 al. 2005; Lathem et al. 2011) that are formed through the condensation of volcanogenic acid
60 solutions of H₂SO₄, HCl and/or HF (Oskarsson 1980; Rose 1977). Such acidic liquid droplets
61 condense on ash surfaces and may rapidly dissolve both glass and mineral constituents
62 (Delmelle et al., 2007; Hoshyaripour et al. 2014). Capillary forces focus thin films of acidic
63 liquids to particle-particle connection points within aggregates causing point-source dissolution
64 (Mueller et al. 2017a, b). Subsequent evaporation of the liquid phase means that these contact
65 points may be bridged between particles by nm- to μm -sized crystals of sulfate and halide salts

66 as the condensed liquid saturates. This type of salt cementation in volcanic ash aggregates
67 occurs within a few seconds during experimental observations (Mueller et al. 2016). We note
68 that low Reynolds numbers were used in these experiments (8-28, see Mueller et al. 2016).
69 These are more applicable to dilute parts of PDCs, such as co-PDC plumes, rather than energetic
70 basal parts (cf. Mueller et al. 2016). On the other hand, these experiments also computed a range
71 of viscous Stokes numbers (St, Ennis et al. 1991) with values ranging between 10^0 and 10^2 .

72 Laboratory experiments suggest a minimum salt concentration of 1800 ppm for efficient
73 cementation of ash aggregates (Mueller et al. 2016). However, natural system salt
74 concentrations involved in aggregate cementation are poorly constrained. This is partly because
75 aggregates are sampled too long after primary deposition so that initial salts may be removed
76 or re-crystallized and replaced during weathering, diagenesis or hydrothermal processes.
77 Furthermore, several factors influence the efficiency of aggregation in nature, including (but
78 not limited to): (1) ash granulometry (fraction of fine ash); (2) available humidity; (3) eruption
79 “acidity” and (4) suspension conditions (e.g., Brown et al. 2012; Mueller et al. 2017a, b;
80 Mueller et al. 2018).

81 In this study we quantify and compare the salt concentrations in natural ash aggregates
82 across different eruptive settings. To explore conditions with a range of humidity and variable
83 possible sources of salts we chose four case study volcanic ash/aggregate settings: (1) “low-
84 salt” dry eruption and dry atmosphere; the 29 December 2013 eruption of Chaparrastique (San
85 Miguel, El Salvador) volcano in a dry atmosphere; (2,3) “intermediate salt” in subaerial
86 eruptions within a humid tropical atmosphere and with involvement of external water; the
87 August 2006 Tungurahua eruption in Ecuador (Douillet et al. 2013; Kueppers et al. 2016) and
88 a 2010 dome collapse event at Soufrière Hills, Montserrat (Stinton et al. 2014; Burns et al.
89 2017); and (4) “high salt” shallow submarine (Surtseyan) 2015 eruption of the Hunga Tonga-
90 Hunga Ha’apai volcano (Colombier et al. 2019). We use the comparison of these settings to
91 explore the variety of possible aggregation processes and relate this, in-turn, to the
92 quantification of suspended ash concentrations during different types of eruption.

93

94 Case studies

95

96 Chaparrastique (San Miguel) volcano

97

98 Chaparrastique is a composite volcano in central-eastern El Salvador with its Summit at 2130
99 m above sea level (a.s.l.). The 29 December, 2013 eruption produced a 9 km-high eruption
100 column that dispersed ash to the west of the volcano (Scarlato et al. 2017). The eruption
101 occurred during the dry season, on a nearly cloudless day, and video footage of the eruption,
102 shot at distances of 8 km, indicates that the eruption commenced with a discrete explosion that
103 rained tephra and ballistics over the summit. This was shortly followed by a larger explosion
104 that produced a pyroclastic density current that travelled ~500 m down the flanks of the volcano
105 before lofting (Scarlato et al. 2017). The eruption then transitioned to a phase characterized by
106 a quasi-steady eruption column that dispersed scoria and ash to the west. Ash lofted from the
107 pyroclastic density current drifted west across the flanks of the volcano and rained out ash
108 aggregates over the western flank. The early explosions may have been driven by interaction
109 between rising magma and groundwater/hydrothermal system in the subvolcanic structure
110 (Scarlato et al. 2017). The aggregates form a framework-supported layer of less than 1-cm thick
111 at the base of the tephra fall deposit. Aggregates represent only 5-10 wt% of the total ash
112 deposit, and were sampled by us in late March/early April 2014.

113

114 Tungurahua volcano

115

116 Tungurahua volcano has its summit at 5017 m a.s.l. and is characterized by a humid tropical
117 atmosphere. We sampled aggregates from the August 2006 eruption was a significant climatic
118 point during an eruptive cycle that started in 1999 (Eycheenne et al. 2012; Wright et al. 2012).
119 This dry magmatic eruption occurred during poor weather/visibility between the 16 and 17
120 August and based on geophysical data lasted for ~8 hours (Kelfoun et al. 2009) with estimated
121 plume heights of 6 to 13 km (Steffke et al. 2010). PDCs generated by column collapse (Steffke
122 et al. 2010) occurred down the NW- and W-flank of the volcano (Douillet et al. 2013). At few
123 locations, the PDCs interacted with the Chambo River at 2000 m a.s.l, locally damming the
124 river for few hours (Kueppers et al. 2016). Aggregates were observed exclusively at the top
125 (fines-poor, clast-supported lapilli tuff) of the 10 meter-thick and commonly massive ash lapilli
126 tuffs, being limited to the top 50 cm of the stratigraphy where they represent less than 5 wt%
127 of the deposit (Kueppers et al. 2016). These aggregates were sampled in August 2009.

128

129 Soufrière Hills volcano

130

131 Soufrière Hills volcano, 1050 m a.s.l., began a new cycle of activity characterized by dome
132 extrusion punctuated by Vulcanian explosions triggered by dome collapse in 2010 (Stinton et
133 al. 2014). On 11 February 2010 at 15:52 (UTC) a northward-directed partial dome collapse (50
134 $\times 10^6$ m³) occurred triggering PDCs that travelled about 1 km offshore and added about 1 km²
135 of land to the island (Stinton et al. 2014). Through entering the ocean and triggering steam
136 explosions, these PDCs produced co-PDC plume deposits containing abundant accretionary
137 lapilli (Stinton et al. 2014), which were used for this study. Hence, these accretionary lapilli
138 deposits are thought to be at the salt rich end of the spectrum, due to their interaction with ocean
139 water. An extensive description of this event and its deposits was carried out by Stinton et al.
140 (2014). The aggregates analyzed were sampled from Mueller et al. (2018) from the Unit III
141 which was a 10 cm thick fall layer, underlain and overlain by massive PDC deposits. The
142 abundance of aggregates decreases from 24 to 2 wt% with increasing distance from the sea
143 (Burns et al. 2017).

144

145 Hunga Tonga- Hunga Ha'apai tuff cone

146

147 The Hunga Tonga- Hunga Ha'apai tuff cone was generated by a series of Surtseyan eruptions
148 that started from a vent at a depth of ~150 m on the floor of the Pacific Ocean 1 km offshore
149 of the islands of Hunga Tonga and Hunga Ha'apai during late 2014-early 2015 (Cronin et al.
150 2017). In a similar fashion to Surtsey (Kokelaar 1986; Cole et al. 2001), the Hunga eruptions
151 progressively became emergent with the latest phases occurring within a water-filled subaerial
152 crater (Cronin et al. 2017), with the deposit being divided into nine units (U1 through U9).
153 Cronin et al (2017) reported a "drying" process during the emergent phase with a gradual
154 decrease in the degree of water-magma interaction. The aggregates consist of scoriaceous lapilli
155 clasts surrounded by ash rims (Colombier et al. 2019), which were sampled on the flanks of the
156 tuff cone (Colombier et al. 2018). Six samples from six different stratigraphic units in the cone
157 were collected during November 2015. Four samples, HH35, HH33, HH28 and HH23, were
158 collected on the south-western flanks ~0.3 km from the center of the vent (in units U1, U3, U6
159 and U7). Instead, sample HH41 was collected on the south-west crater rim (<0.2 km from the
160 vent) and corresponds to unit U9; and HH50 was sampled 1.4 km to the north of the vent center
161 on the northern coastline and corresponds to the uppermost part of unit U6. Sample HH50
162 differs from the other samples as it is more distal and consists of an ash-rich layer with few

163 lapilli and might represent a more energetic eruptive pulse. The stratigraphic units studied here
164 represent a portion of the emergent phase of the eruption leading to the building of the tuff cone.
165 Although the water depth likely decreased during the eruptive sequence, the vent remained
166 below sea level throughout the entire eruption, yet became isolated from the ocean at the end
167 of the eruption (Cronin et al. 2018; Garvin et al. 2018). The water in the eruptive vent was
168 mainly seawater, possibly chemically modified by interaction with the vent system, rain-fall
169 runoff and leachates from the growing cone around it. In this regard, the tuff cone was subject
170 to significant rain immediately after the cessation of eruptive activity in January 2015, leading
171 to a well-developed erosional rill network (Cronin et al. 2017). Surface run-off may have
172 reduced efficient percolation of rain water so that these samples appear only weakly leached.
173 Aggregates are ubiquitous in the deposit, making up >90 wt% of the lapilli fraction (Colombier
174 et al. 2019).

175

176 **Methodology**

177 Field work and sampling of the aggregates from Chaparrastique volcano were conducted in late
178 March/early April 2014 before the deposit had been washed out by rain. Aggregates were
179 sampled at a distance of ~1 km from the vent in the western flank. The internal structure and
180 grain size of these aggregates were analyzed using back-scattered electron images (SU 5000
181 Schottky FE-SEM, HITACHI). Aggregates from other volcanoes were available from previous
182 studies.

183 Aqueous leaching was used to determine surface salt concentration of ash aggregates
184 from the different deposits. For each volcano, use of several aggregates was necessary in order
185 to collect enough ash particles for the leaching analysis. We mechanically crushed aggregates
186 and immersed fine to coarse grained ash particles in deionised water for one hour at
187 solid:solution ratios of 1:100, 1:500 and 1:1000 (Table 1). For Soufrière Hills and Tungurahua
188 volcanoes, we also analyzed non-aggregated material (loose matrix ash) in which the aggregates
189 were embedded. Water extracts were filtered through a 0.2 µm cellulose-acetate membrane
190 filter and analyzed for Cl⁻ and SO₄²⁻ in a Dionex 2000 ion chromatograph with an IonPac AS14
191 anion exchange column at the Université catholique de Louvain, Belgium. Concentrations of
192 Al, Ca, Fe, K, Mg, Mn, and Si in leachate solutions were also determined by inductively coupled
193 plasma atomic emission spectrometry (ICP-AES) at the Université catholique de Louvain.
194 Short-term analytical precision (repeatability) is better than 5% for the ion chromatography and
195 ICP-AES analyses.

196 In addition, we performed chemical mapping and morphological observations on the ash
197 particles from various aggregates from sample HH33 of Hunga Tonga-Hunga Ha'apai using a
198 Hitachi SU 5000 Scanning electron microscope (SEM) at Ludwig Maximilian University of
199 Munich, Germany. We carefully removed the ash grains from these aggregates in order to avoid
200 complete disaggregation and to preserve particle clusters with binding salts. Five of these
201 particle agglomerates were chemically mapped.

202 A forward model was used to predict the sequence of salts precipitating during
203 equilibrium evaporation of seawater with an average composition (Stumm and Morgan 1996).
204 The calculations were performed with the open-source geochemical code PHREEQC 3.4 and
205 using Pitzer's equations for solute activities at high ionic strength (Parkhurst and Appelo 1999)
206 at a temperature of 70°C. The model allows precipitation (and possibly redissolution) of
207 carbonate, sulfate and chloride salts, including anhydrite (CaSO₄), gypsum (CaSO₄·2H₂O),
208 halite (NaCl), sylvite (KCl), bischofite (MgCl₂·6H₂O), glauberite (Na₂Ca(SO₄)₂), kieserite
209 (MgSO₄·H₂O), polyhalite (K₂MgCa₂(SO₄)₄·2H₂O), hexahydrate (MgSO₄·6H₂O) and epsomite
210 (MgSO₄·7H₂O).

211

212 Results

213 Aggregate types and characteristics

214

215 At Chaparrastique, the whitish aggregates are up to 10 mm in diameter and predominantly
216 consist of poorly-structured ash pellets with few armored lapilli. The ash particles in these
217 agglomerates range in size from ~ 1 to 400 µm in diameter. At Tungurahua volcano, the
218 aggregates are up to 8 mm in diameter and consist of pellets pyroclasts made of grains ranging
219 between <1-200 µm in diameter (Mueller et al. 2018). Aggregates at Soufrière Hills were
220 described in detail by Burns et al. (2017) and further analyzed by Mueller et al. (2018) for
221 particle size distribution. All are accretionary pellets with concentric structure and densities (ρ)
222 and porosities (Φ) of 1300-1900 kg.m⁻³ and 0.3-0.5, respectively (Burns et al. 2017). The
223 aggregates range in diameter between 5 and 11 mm with ash grain sizes typically <200 µm
224 (Mueller et al. 2018). Aggregates at the Hunga Tonga- Hunga Ha'apai tuff cone are essentially
225 juvenile lapilli surrounded by an ash rim. Such particles would be termed "coated particles"
226 using the nomenclature of Brown et al. (2012). However, we recently showed that a significant
227 fraction of the ash grains from the rim were formed in situ by granulation of the core caused by
228 thermal stress rather than by aggregation of external ash particles (Colombier et al. 2019). This

229 means that ash encasement is not always diagnostic of ash aggregation in the deposits from
230 Surtseyan eruptions. Additional aggregation of external particles was however not ruled out.
231 Hereafter, we will use the term aggregate for simplicity but it should be kept in mind that the
232 formation mechanism of ash rims during Surtseyan eruptions may differ from other cases. The
233 density and porosity of the aggregates are largely controlled by those of the central lapilli with
234 values of ρ and Φ ranging between 300-1800 kg.m⁻³ and 0.35-0.89, respectively. The size of
235 the aggregates at Hunga Tonga- Hunga Ha'apai varies between 2 and 5 mm with ash particles
236 typically smaller than a few hundreds of μm (Colombier et al. 2019).

237

238 Leaching analysis

239

240 The raw data of concentrations for anions and cations in aggregated and non-aggregated
241 material analyzed are given in Table 1 and are summarized for all aggregates in Figure 1. The
242 concentrations of Cl⁻, Na, SO₄²⁻, Ca, Mg and K evolve in a similar pattern between the
243 aggregates from different settings and typically increase between our sites in the order:
244 Chaparrastique < Tungurahua < Soufrière Hills < Hunga Tonga-Hunga Ha'apai (Fig. 1). In all
245 cases, leachate concentrations are systematically higher in the aggregates than in non-
246 aggregated ash (Table 1).

247

248 SEM observations and chemical mapping

249

250 Chemical mapping of aggregates from the HH33 sample of Hunga Tonga-Hunga Ha'apai, that
251 had the highest leachate concentrations (Table 1), reveals the presence of several different salt
252 phases at the ash surface and at the contact between ash particles (Fig. 2). Chemical mapping
253 and crystal form were used for identification. The most abundant salts are NaCl and Ca₂SO₄,
254 with KCl and MgCl₂ being much less abundant. NaCl and CaSO₄ crystals are the coarsest,
255 ranging between 5-50 μm , while the less common salts are <5 μm in diameter. Relationships
256 of 1:1 for the molar concentrations of NaCl and CaSO₄ confirms the SEM observations that
257 these are the most abundant at Hunga Tonga-Hunga Ha'apai (Fig. 3). No similar stoichiometric
258 trend is observed for the molar concentrations of other anion-cation pairs at Hunga Tonga-
259 Hunga Ha'apai.

260

261 Model of salt precipitation

262

263 The evolution of the saturation state of seawater with respect to carbonate, sulfate and chloride
264 salts during evaporation is shown in Figure 4. Calcite precipitates immediately upon
265 evaporation. Anhydrite starts to precipitate at a concentration factor of **around three** (i.e. **after**
266 **~24%** of evaporation), followed by halite at a concentration factor of **~11** (i.e. **after** **~91%** of
267 evaporation) and then glauberite. Sylvite and kieserite precipitate when evaporation is almost
268 complete (**after** **>98%** of evaporation).

269

270 **Discussion**

271 We first consider Surtseyan eruptions and how salt concentrations may evolve during
272 progressive emergence and “drying” of eruptions. Secondly, we examine the process of salt
273 precipitation on ash surfaces for a spectrum of “dry or low-salt” to “intermediate” and “wet or
274 high-salt” eruption types. **Finally**, we generalize our findings to propose a conceptual model
275 linking salt precipitation to eruptive scenario and the implications for ash dispersal and ash fall
276 hazards.

277

278 Salt precipitation during Surtseyan eruptions

279

280 The concentrations of Na, Cl⁻, Ca, SO₄²⁻, Mg and K are higher in aggregates from Hunga Tonga-
281 Hunga Ha’apai than **for** Soufrière Hills, Tungurahua and Chaparrastique (in this order). To our
282 knowledge, the maximum concentrations in Na, Cl⁻ and K found in these aggregates are, to
283 date, the highest values found by leaching analysis of volcanic material (see [Witham et al. 2005](#)
284 and [Ayrís and Delmelle 2012](#) for compilations).

285 Diagrams comparing the concentrations of these anions and cations allow **us** to represent
286 the traces of evaporation of seawater brines ([Babel and Schreiber 2014](#)). We observed a 1:1
287 relationship for the molar concentrations of Na-Cl and Ca-SO₄, consistent with NaCl and CaSO₄
288 seen in SEM (Fig. 3). Although K-Cl and Mg-Cl salts were observed during SEM analysis, their
289 contribution to the total Cl⁻ content is negligible because of their low volumetric concentration
290 (Fig. 2).

291 The Hunga Tonga-Hunga Ha'apai aggregates were sampled 10 months after deposition.
292 There must have been some rainfall leaching so that the reported values are conservative
293 estimates of primary salt precipitation in a volcanic plume, which will be favored by the
294 temperature, salinity and humidity conditions during a Surtseyan eruption. A significant amount
295 of seawater is contained in Surtseyan plumes and the high thermal budget likely drives it to
296 rapidly boil, evaporate and concentrate into a pervasive brine causing salt precipitation.
297 Hovland et al. (2006) showed that evaporation associated with boiling is rapid and highly
298 productive. The extreme conditions of salinity, humidity, temperature, and high mobility of the
299 seawater in Surtseyan settings probably contribute to the extensive salt precipitation observed
300 here. Salts likely precipitate in the brine-soaked aggregates while they remain in the plume.
301 Further, aggregates once formed could be re-coated by brine during transport in the plume, as
302 well as after deposition. Once deposited, further burial by wet tephra accumulating above may
303 cause brine to percolate downwards. In this way successive episodes of evaporation and
304 precipitation could explain the concentrations in excess of those of seawater (Table 1).
305 Additional primary salt precipitation by gas scavenging likely occurs but appears to be
306 overwhelmed by seawater evaporation-induced precipitation.

307 The equilibrium evaporation calculations, leachate data and SEM analyses all point to the
308 presence of CaSO_4 and NaCl salts in the ash aggregates. As illustrated in Figure 4, precipitation
309 of sulfate and chloride salts on the ash surfaces required between 20 and 90 % of evaporation
310 of seawater droplets. Although the model results predict that calcite is stable, carbonate salts
311 were not observed in the ash aggregates. In contrast to sulfate and chloride salts, the low-pH
312 conditions imparted by the volcanic gas condensates to the liquid phase within the eruption
313 plume probably prevented precipitation/preservation of carbonates. Minor amounts of
314 potassium chloride salts are shown in the SEM analysis, consistent with the modelled
315 appearance of sylvite after almost complete brine evaporation (Fig. 4).

316 Variations in the anion and cation concentrations through the eruptive sequence also show
317 the dominance of primary seawater evaporation during the Hunga Surtseyan eruption (Fig. 5).
318 Secondary depletion of salts due to dissolution by rainwater alone cannot explain why some
319 stratigraphic units are depleted and others not. Figure 5 shows an overall decrease of Na and
320 Cl^- contents through the eruptive sequence (with the exception of sample HH50 from unit 6
321 which is enriched in these elements). The evolution of Ca and SO_4^{2-} is similar except for the
322 last (highest) stratigraphic level sample, unit 8, which is enriched in CaSO_4 .

323 This concentration pattern might reflect: (i) variable volumes of seawater involved during
324 each eruptive phase sampled here; (ii) variable efficiency of seawater evaporation during the
325 eruption sequence; or (iii) changes in the seawater composition. As the eruption progressed, it
326 clearly became emergent (Cronin et al. 2017), thus less and less seawater was entrained in the
327 plume. On the one hand, this “drying” process favors more efficient seawater evaporation
328 because the particles stay hotter for longer due to the lower water:pyroclast ratios. However,
329 the lower volumes of seawater entrained in the plume during emergence are likely responsible
330 for the overall decrease in salt concentrations with height of the stratigraphy. These results
331 hence suggest an overall decreasing degree of magma-water interaction during progressive
332 emergence, in agreement with Cronin et al. (2017).

333 It was also observed from detailed studies of eruption footage of the Hunga Tonga-Hunga
334 Ha’apai eruption (Taniela Kula; pers. comm.) that there were repeated partial collapses of the
335 southern flank of the tuff cone and re-opening of the crater to the sea during the eruption. This
336 likely caused sporadic renewed entry of seawater explaining why some intermediate units could
337 be enriched in salts (e.g., sample HH50; Fig. 5). That the uppermost stratigraphic unit (sample
338 HH41; Fig. 5) has a higher CaSO₄/NaCl than other units could also be due to rainfall leaching
339 and the higher relative solubility of NaCl. Additional influences for these observed variations
340 could be related to eruption of any hydrothermally-altered materials from the conduit as the
341 eruption progressed. However, this does not appear to be the case at Hunga, because no
342 evidences of hydrothermal clasts were found in any of the tephtras.

343 Similar S- and Cl- bearing sea salts were reported within Soufrière Hills aggregates and
344 likely further promoted aggregate cementation in the Co-PDC plumes (Burns et al. 2017).
345 Morgavi et al. (2019) also recently proposed that high concentrations of seawater salts had a
346 strong influence on aggregate cementation and resistance to breakage during the 7000 yrs. BP
347 eruption of Secche di Lazzaro in Italy.

348

349 Salt precipitation and implications for aggregates in other settings

350

351 Our data show that precipitation occurs in a range of eruptive scenarios, from dry eruptions
352 with only atmospheric humidity available for aggregation, to an oversupply of water during a
353 Surtseyan eruption and resulting tephra-brine interaction (Fig. 6). Intermediate cases involve
354 subaerial eruptions involving groundwater or PDCs entering the sea. Using our quantitative

355 dataset of salt concentrations in volcanic ash aggregates, we estimate here the minimum salt
356 concentration needed for cementation.

357 Aggregates are preserved in the deposits from all eruptions examined, even with low total
358 salt concentrations. With only <100 ppm for the “low-salt” Chaparrastique aggregates this is
359 far lower than the threshold **needed for aggregation** suggested by laboratory-scale experiments
360 (>1800 ppm; [Mueller et al. 2016](#)). For Chaparrastique volcano (salt-poor setting), the low salt
361 concentrations are likely produced by the interaction of volcanic gas with atmospheric humidity
362 or groundwater. We **can** also show that aggregate material has higher salt concentrations than
363 non-aggregated free particles from the surrounding matrix in which the aggregates are
364 embedded. This may reflect that the distribution of salts in the plume/PDC is not homogenous
365 and permanent aggregation may only occur in particles in the **salt-concentration** zones. It may
366 represent particular spatial mechanism for concentrating salts during an eruption (e.g.,
367 explosive interactions at the margins of a conduit or at the outer margins of a PDC entering
368 water). Alternatively, it may represent short-lived conditions during an eruption as magma-
369 water ratios vary or as vent conditions and atmospheric conditions change.

370 A minimum salt volume is therefore required to produce aggregates that survive transport
371 and deposition. The ratio of aggregated to non-aggregated material might be related to the
372 eruptive setting (amount of external water and salt source), the abundance and nature of the
373 volcanic eruptive gas phase and secondary processes such as rain water influencing the salt
374 content in the tephra after deposition. Additional factors such as the amount of degassing, the
375 intensity of the eruption, the grain size distribution, the degree and duration of interaction of
376 the tephra with volcanic gas, the occurrence of hydrothermal alteration prior to an eruption and
377 the presence of a crater lake might also control the amount of salt precipitation and the aggregate
378 stability ([Armienta et al. 2002](#); [Cronin et al. 2003](#)).

379 Regarding the high salt concentrations found here for a seawater setting, we stress that
380 high values of SO_4^{2-} and Cl^- have also been reported at other volcanoes (Figure 1). As an
381 example, [Cronin et al. \(2003\)](#) found SO_4^{2-} contents **s of** up to 31000 ppm in tephra layers from
382 phreatomagmatic phases of the 1995-1996 Ruapehu eruption. Recently, [Damby et al. \(2018\)](#)
383 **reported** the highest values for SO_4^{2-} ever found in volcanic leachates, **with concentrations of**
384 up to 85000 ppm **being recorded** in ash deposits from the 2018 Kilauea eruption. The high
385 concentrations in the cases of Ruapehu were attributed to the presence of an acidic crater lake
386 and hydrothermal alteration prior to the eruption ([Cronin et al. 2003](#)). In the case of Kilauea,
387 the very high values for SO_4^{2-} **may** partly be explained by the massive sulfur dioxide (SO_2)

388 emissions (of up to 50,000 tons per day; Neal et al. 2018) leading to chemical reactions between
389 ash and the SO₂-rich plume causing the formation of calcium sulfates. The highest Cl⁻ values
390 after those presented here for Hunga Tonga-Hunga Ha'apai were found in ash samples from
391 Irazú volcano in Costa Rica (Taylor and Stoiber 1973). These high concentrations at Irazú might
392 be explained by solfataric alteration (Taylor and Stoiber 1973) and/or enrichment by rain or the
393 presence of a crater lake (Murata et al. 1966).

394

395 Implications for ash plume dispersal modelling and natural hazards

396

397 One of the key unknowns regarding aggregation in ash plume dispersal models involves
398 aggregate break-up processes. Currently, models regard all aggregates as ash material which is
399 quantitatively removed from the atmosphere (Folch et al. 2010). However, both experimental
400 approaches (Mueller et al. 2017a, b) and *in-situ* field observations (Taddeucci et al. 2011;
401 Bonadonna et al. 2011; Bagheri et al. 2016) clearly demonstrate the fragile nature of aggregates.
402 Thus, we must infer that only a fraction of aggregates will be deposited as such. Whereas the
403 process of aggregation can happen without any salt but with the mere presence of humidity
404 (Mueller et al. 2016; Van Eaton et al. 2012; Schumacher and Schminke 1991; Gilbert and Lane
405 1994), the stability of aggregates, and therefore preservation chances increase with the amount
406 of salts present as cementation agent. Experiments have shown that both the amount and
407 presence of soluble salt compounds on ash surfaces can be derived from various eruption
408 parameters, such as degassing rate or magma chemistry (Ayrís et al. 2013, 2014; Delmelle et
409 al. 2018).

410 Our study is the first to cover such a wide range of possible salt concentrations in volcanic
411 ash aggregates, which represent a wide variety of eruptive settings as well as degrees of fresh
412 and/or saltwater involvement. These data combined with recent experimental results (Mueller
413 et al. 2017a, b), thus provide a resource for the consideration of aggregate stability and break-
414 up in ash plume dispersal modelling. In experimental results, only about 50 wt.% of ash
415 aggregates survived impact at terminal fall velocity at salt concentrations of 2000 ppm. Only at
416 concentrations exceeding 50000 ppm, did 100 wt.% of ash aggregates survive impacts at
417 terminal fall velocities. These experimental results are consistent with our observations on
418 natural deposits. At Chaparrastique and Tungurahua, aggregates represent a low portion of the
419 fall deposit (5-10 wt%), likely indicating both a lower aggregation rate related to low humidity,
420 and a lower stability and higher break-up of the aggregates induced by the low salt

421 concentrations. On the other hand, all lapilli formed during **the** Surtseyan eruption at Hunga
422 Tonga-Hunga Ha'apai preserved ash rims after deposition. Although some particles might have
423 been lost from the ash rims, this suggests that stability of these aggregates comes close to 100 %
424 due to the extremely high salt contents (tens of thousands of ppm), **a conclusion which is** also
425 in agreement with **the** experiments of [Mueller et al. \(2017a, b\)](#). At Soufrière Hills, [Burns et al.](#)
426 [\(2017\)](#) demonstrated that the abundance of aggregates decreases from 24 to 2 wt% as distance
427 from the sea increases, further illustrating the role of sea salt concentration on the cementation
428 and preservation of aggregates in the deposits. However, it is important to note that in all **of**
429 these natural settings, additional parameters such as duration of transport, settling velocity,
430 grain size and morphology of the aggregates, **as well as** the time of sampling after deposition,
431 might influence the preservation of the aggregates during transport and deposition, and the salt
432 concentrations. Additional data is therefore required to clearly quantify the link between salt
433 concentration and aggregate abundance in natural deposits.

434 This study highlights the necessity for ash plume models to **treat** break-up processes of
435 ash aggregates **differently** in distinct volcanic settings. Aggregates from eruptions that do not
436 have any significant external salt source involved such as seawater, crater lake or hydrothermal
437 systems ([Cronin et al. 2003](#); [Witham et al. 2005](#)), exhibit salt concentrations well below 1000
438 ppm ([Chaparrastique, Tungurahua](#), see Fig. 1). Paired with experimental results, this means that
439 aggregates found in these deposits represent only a portion of the original number formed in
440 the plume. Consequently, we infer that only a portion of aggregates incorporated in **numerical**
441 **ash plume** models are **actually** removed from the atmosphere by aggregate deposition. The
442 remaining portion is likely to stay airborne and become re-entrained into the dispersal process.
443 Considering the volcanic setting, and in particular the humidity and abundance of external salt
444 sources, will help to estimate the order of magnitude of aggregation rate, salt concentration and
445 subsequent aggregate abundance and stability in volcanic plumes. Real time leaching analysis
446 of ash and aggregates during eruptive crises might **thus** provide a valuable tool for plume
447 forecast modelling, **especially** regarding the efficiency of atmospheric ash removal through
448 aggregation. We anticipate that our new findings may **thus** represent a **resource** for the
449 consideration of eruption source parameters (ESPs, [Mastin et al. 2010](#)) in ash dispersal
450 modelling in which break-up processes in ash plume modelling, while **being** recognized, have
451 not yet been quantified ([Folch et al. 2010](#)).

452 Finally, **our** results **can also be useful** to efforts to constrain the concentrations of soluble
453 salts in a range of eruptive settings for the analysis of secondary remobilization of these salts
454 **which** affects water resources, agriculture and human health ([Damby et al. 2018](#)). After

455 deposition, the ash deposits can interact with water leading to dissolution of the salts causing,
456 for instance, contamination of drinking water (Damby et al. 2018). Here, the survival of ash
457 aggregates is a constraint that contributes to the accurate forecasting of such secondary risks.

458

459 **Conclusion**

460

461 We here move towards a general, data-driven model for the process of particle binding by salt
462 formation that covers a wide spectrum of eruptive scenarios ranging from dry, salt-poor
463 magmatic eruptions to high humidity, salt-rich Surtseyan eruptions (and including intermediate
464 cases). Key findings of our study include:

- 465 1. Variations in salt concentrations during volcanic eruptions can result from fresh and/or
466 saltwater precipitation, gas scavenging, hydrothermal alteration and/or interaction with
467 rain water.
- 468 2. An increase in the amount of salt sources in the vicinity of the vent or the transported
469 tephra may lead to a dramatic increase in salt concentration promoting a greater stability
470 of the aggregates.
- 471 3. The formation and survival of aggregates are ubiquitous during Surtseyan eruptions
472 occurring in seawater due to both the high humidity and pervasive salt precipitation
473 during such eruptions. This was confirmed by the very high salt concentrations found
474 in the aggregates from the Hunga Tonga- Hunga Ha'apai 2014-2015 Surtseyan eruption.
- 475 4. The concentration of salts varies with stratigraphic height in tuff cones, with an overall
476 reduction in salt content. This might reflect the progressive emergence during Surtseyan
477 eruptions and decreasing volumes of seawater involved with time.
- 478 5. At a given volcano with specific aggregate characteristics and time of sampling after
479 deposition, aggregates contain systematically more salts than non-aggregated particles.
480 This implies that aggregates will only survive up to deposition when they contain a
481 sufficient amount of salts.

482 Future studies focusing on a quantitative correlation between humidity, salt concentration
483 and aggregate abundance in volcanic plumes and associated deposits will allow establishment
484 of a link between volcanic eruption style (controlling grain size, abundance and nature of
485 volcanic gas, suspension conditions), volcanic setting (controlling external salt sources and
486 humidity), and aggregate abundance and preservation in volcanic plumes. This knowledge,
487 coupled with systematic real time leaching analysis during volcanic eruptions may provide key

488 information on the concentration, stability and longevity of aggregates to be incorporated in ash
489 plume dispersal models with far reaching implications for hazards related to populations and
490 air traffic. Our results suggest that water and salt-rich volcanic settings, such as those during
491 Surtseyan eruptions, will favor higher aggregate concentration and stability in volcanic plumes,
492 likely enhancing proximal tephra deposition. Real time measurements of salt concentrations in
493 shallow subaqueous environments could also shed light on the possible evolution toward dry
494 magmatic phases during emergent phases.

495

496 **Acknowledgements**

497 MC and DBD acknowledge support from an ERC Advanced Grant (Explosive Volcanism in the
498 Earth System: EVOKES - 247076). UK and SM acknowledge financial support by the
499 European Commission (FP7-MC-ITN grant number 607905: VERTIGO). UK acknowledges
500 financial support from grant KU2689/2-1 from the Deutsche Forschungsgemeinschaft. SJC and
501 MT acknowledge funding support from the School of Environment and the Faculty
502 Development Research Fund of the University of Auckland. MC and SBM are grateful to Koni
503 for inspirational thoughts about this paper. We also thank the editor Andrew Harris, the associate
504 editor Laura Pioli as well as Eduardo Rossi and an anonymous reviewer for discussions that
505 contributed to substantial improvement of our initial manuscript.

506

507 **References**

- 508 Alois S, Merrison J, Iversen JJ, et al. (2017) Contact electrification in aerosolized
509 monodispersed silica microspheres quantified using laser-based velocimetry. *J Aerosol*
510 *Sci* 106:1–10. doi: 10.1016/j.jaerosci.2016.12.003
- 511 Armienta MA, La Cruz-Reyna SD, Morton O, et al. (2002) Chemical variations of tephra-fall
512 deposit leachates for three eruptions from Popocatepetl volcano. *J Volcanol Geotherm*
513 *Res* 113:61–80. doi: 10.1016/S0377-0273(01)00251-7
- 514 Ayris PM, Delmelle P (2012) The immediate environmental effects of tephra emission. *Bull*
515 *Volcanol* 74:1905–1936. doi: 10.1007/s00445-012-0654-5
- 516 Ayris PM, Lee A, Wilson K, et al. (2013) SO₂ sequestration in large volcanic eruptions: high-
517 temperature scavenging by tephra. *Geochim Cosmochim Acta* 110:58–69. doi:
518 10.1016/j.gca.2013.02.018

- 519 Ayris PM, Delmelle P, Maters EC, et al. (2014) HCl uptake by volcanic ash in the high
520 temperature eruption plume: mechanistic insights. *Geochim Cosmochim Acta* 144:188–
521 201. doi: 10.1016/j.gca.2014.08.028
- 522 Babel M, Schreiber BC (2014) *Geochemistry of evaporites and evolution of seawater:*
523 *Treatise on Geochemistry*. Second Edition, Elsevier Ltd. 488–544. doi:10.1016/b978-0-
524 08-095975-7.00718-x
- 525 Bagheri G, Rossi E, Biass S, et al. (2016) Timing and nature of volcanic particle clusters
526 based on field and numerical investigations. *J Volcanol Geotherm Res.* 327, 520–530.
527 doi: 10.1016/j.jvolgeores.2016.09.009
- 528 Bonadonna C, Genco R, Gouhier M, et al. (2011) Tephra sedimentation during the 2010
529 Eyjafjallajökull eruption (Iceland) from deposit, radar, and satellite observations. *J*
530 *Geophys Res* 116, B12202. doi: 10.1029/2011JB008462
- 531 **Brown RJ, Bonadonna C, Durant AJ (2012) A review of volcanic ash aggregation. *Phys Chem***
532 ***Earth* 45–46:65–78. doi: 10.1016/j.pce.2011.11.001**
- 533 Burns FA, Bonadonna C, Pioli L, et al. (2017) Ash aggregation during the 11 February 2010
534 partial dome collapse of the Soufriere Hills Volcano, Montserrat. *J Volcanol Geotherm*
535 *Res* 335:92–112. doi: 10.1016/j.jvolgeores.2017.01.024
- 536 Cole P, Guest J, Duncan A, et al. (2001) Capelinhos 1957-1958, Faial, Azores: deposits formed
537 by an emergent surtseyan eruption. *Bull Volcanol* 63:204–220. doi:
538 10.1007/s004450100136
- 539 Colombier M, Scheu B, Wadsworth FB, et al. (2018) Vesiculation and Quenching During
540 Surtseyan Eruptions at Hunga Tonga-Hunga Ha’apai Volcano, Tonga. *J Geophys Res*
541 *Solid Earth* 123:3762–3779. doi: 10.1029/2017JB015357
- 542 Colombier M, Scheu B, Kueppers U, et al. (2019) In situ granulation by thermal stress during
543 Subaqueous volcanic eruptions. *Geology* 47:179–182. doi:
544 10.1130/G45503.1/4607844/g45503
- 545 Costa A, Macedonio G, Folch A (2006) A three-dimensional Eulerian model for transport and
546 deposition of volcanic ashes. *Earth Planet Sci Lett* 241:634–647. doi:
547 10.1016/j.epsl.2005.11.019

548 Costa A, Folch A, Macedonio G (2010) A model for wet aggregation of ash particles in volcanic
549 plumes and clouds: 1. Theoretical formulation. *J Geophys Res* 115:1–14. doi:
550 10.1029/2009JB007175

551 Cronin, S. J., M. Brenna, I. E. M. Smith, et al (2017) New volcanic island unveils explosive
552 past, *Eos*, 98. doi: 10.1029/2017EO076589

553 Cronin SJ, Neall VE, Lecointre JA, et al. (2003) Environmental hazards of fluoride in volcanic
554 ash: A case study from Ruapehu volcano, New Zealand. *J Volcanol Geotherm Res*
555 121:271–291. doi: 10.1016/S0377-0273(02)00465-1

556 Damby DE, Peek S, Lerner AH, et al. (2018) Volcanic ash leachate chemistry from increased
557 2018 activity of Kīlauea Volcano, Hawaii: U.S. Geological Survey data release,
558 <https://doi.org/10.5066/P98A07DC>.

559 Del Bello E, Taddeucci J, Scarlato P, et al. (2015) Experimental investigation of the
560 aggregation-disaggregation of colliding volcanic ash particles in turbulent, low-humidity
561 suspensions. *Geophys Res Lett* 1068–1075. doi: 10.1002/2014GL062292

562 Delmelle P, Pelletier M (2005) Surface area, porosity and water adsorption properties of fine
563 volcanic ash particles. *Bull Volcanol* 67:160–169. doi: 10.1007/s00445-004-0370-x

564 Delmelle P, Lambert M, Dufrêne Y, et al. (2007) Gas/aerosol-ash interaction in volcanic plumes:
565 New insights from surface analyses of fine ash particles. *Earth Planet Sci Lett* 259:159–
566 170. doi: 10.1016/j.epsl.2007.04.052

567 Delmelle P, Wadsworth FB, Maters EC, et al. (2018) High Temperature Reactions Between
568 Gases and Ash Particles in Volcanic Eruption Plumes. *Reviews in Mineralogy and*
569 *Geochemistry* 84:285–308. doi: 10.2138/rmg.2018.84.8

570 Douillet GA, Tsang-Hin-Sun È, Kueppers U, et al. (2013) Sedimentology and geomorphology
571 of the deposits from the August 2006 pyroclastic density currents at Tungurahua volcano,
572 Ecuador. *Bull Volcanol* 75:765. doi: 10.1007/s00445-013-0765-7

573 Draxler RR, Hess GD (1997) Description of the HYSPLIT4 Modeling system. NOAA Tech
574 Mem ERL ARL-224.

575 Ennis BJ, Tardos G, Pfeffer R (1991) A microlevel-based characterization of granulation
576 phenomena. *Powder Technol* 65:257–272

- 577 Eychenne J, Le Pennec J-L, Troncoso L, et al (2012) Causes and consequences of bimodal
578 grain-size distribution of tephra fall deposited during the August 2006 Tungurahua
579 eruption (Ecuador). *Bull Volcanol* 74:187–205. doi: 10.1007/s00445-011-0517-5
- 580 Folch A, Costa A, Durant A, et al. (2010) A model for wet aggregation of ash particles in
581 volcanic plumes and clouds: 2. Model application. *J Geophys Res* 115:1–16. doi:
582 10.1029/2009JB007176
- 583 Garvin JB, Slayback DA, Ferrini V, et al. (2018) Monitoring and Modeling the Rapid Evolution
584 of Earth's Newest Volcanic Island: Hunga Tonga Hunga Ha'apai (Tonga) Using High
585 Spatial Resolution Satellite Observations. *Geophys Res Lett* 45:3445–3452. doi:
586 10.1002/2017GL076621
- 587 Gilbert JS, Lane SJ (1994) The origin of accretionary lapilli. *Bull Volcanol* 56:398–411. doi:
588 10.1007/BF00326465
- 589 Hoshyaripour G, Hort M, Langmann B (2014) Ash iron mobilization in volcanic eruption
590 plumes. *Atmosph. Chem Phys Disc* 14:32535–3258.
- 591 Hovland M, Rueslatten HG, Johnsen HK, et al. (2015) Salt formation associated with sub-
592 surface boiling and supercritical water. *Mar Pet Geol* 23:855–869. doi:
593 10.1016/j.marpetgeo.2006.07.002
- 594 James MR, Gilbert JS, Lane SJ (2002) Experimental investigation of volcanic particle
595 aggregation in the absence of a liquid phase. *J Geophys Res* 107:1–13. doi:
596 10.1029/2001JB000950
- 597 Kelfoun K, Samaniego P, Palacios P, et al. (2009) Testing the suitability of frictional behaviour
598 for pyroclastic flow simulation by comparison with a well-constrained eruption at
599 Tungurahua volcano (Ecuador). *Bull Volcanol*. doi: 10.1007/s00445-009-0286-6
- 600 Kueppers U, Ayris P, Bernard B, et al. (2016) Volcano vs. environment: Where, when and why
601 does ash aggregate? *Cities on Volcanoes* 9, November 2016, Puerto Varas, Chile
- 602 Kokelaar P (1986) Magma-water interactions in subaqueous and emergent basaltic volcanism.
603 *Bull Volcanol* 1:275–289
- 604 Latham TL, Kumar P, Nenes A, et al. (2011) Hygroscopic properties of volcanic ash. *Geophys*
605 *Res Lett* 38:2–5. doi: 10.1029/2011GL047298

- 606 Mastin LG, Guffanti M, Servranckx R, et al. (2009) A multidisciplinary effort to assign realistic
607 source parameters to models of volcanic ash-cloud transport and dispersion during
608 eruptions. *J Volcanol Geotherm Res* 186:10–21. doi: 10.1016/j.jvolgeores.2009.01.008
- 609 Morgavi D, Valentini L, Porreca M, et al (2019) Volcanic ash aggregation enhanced by
610 seawater interaction: the case of the Secche di Lazzaro phreatomagmatic deposit (
611 Stromboli). *Ann Geophys* 61:. doi: 10.4401/ag-7874
- 612 Mueller SB, Kueppers U, Ayris PM, et al. (2016) Experimental volcanic ash aggregation:
613 Internal structuring of accretionary lapilli and the role of liquid bonding. *Earth Planet Sci*
614 *Lett* 433:232–240. doi: 10.1016/j.epsl.2015.11.007
- 615 Mueller SB, Ayris PM, Wadsworth FB, et al. (2017) Ash aggregation enhanced by deposition
616 and redistribution of salt on the surface of volcanic ash in eruption plumes. *Scientific*
617 *reports*, 7, 45762. doi: 10.1038/srep45762
- 618 Mueller SB, Kueppers U, Ametsbichler J, et al. (2017) Stability of volcanic ash aggregates and
619 break-up processes. *Sci Rep* 7:1–11. doi: 10.1038/s41598-017-07927-w
- 620 Mueller SB, Kueppers U, Huber MS, et al (2018) Aggregation in particle rich environments :
621 a textural study of examples from volcanic eruptions , meteorite impacts , and fluidized
622 bed processing. *Bull Volcanol* 80:32. doi: 10.1007/s00445-018-1207-3
- 623 Murata K., Dondoli C, Saenz R (1966) The 1963-65 Eruption of Iraziti Volcano, Costa Rica
624 (The period of March 1963 to October 1964). *Bull Volcanol* 29:763
- 625 Neal CA, Brantley SR, Antolik L, et al (2018) The 2018 rift eruption and summit collapse of
626 Kīlauea Volcano. *Science* (80-) 363:367–374. doi: 10.1126/science.aav7046
- 627 Oskarsson N (1980) The interaction between volcanic gases and tephra: fluorine adhering to
628 tephra of the 1970 Hekla eruption. *J Volcanol Geotherm Res* 8:251-266.
- 629 Parkhurst DL, Appelo CAJ (1999) Users guide to PHREEQC (version 2) - a computer program
630 for speciation, reaction-path, 1D-transport, and inverse geochemical calculations. US
631 Geological Survey Water Resources Investigations Report 99–4259:312p
- 632 Rose WI (1977) Scavenging of volcanic aerosol by ash: atmospheric and volcanologic
633 implications. *Geology* 5:621–624.

- 634 Salman AD, Hounslow MJ, Seville JPK (2006) Handbook of Powder Technology –
635 Granulation, eleventh Ed. Elsevier, Amsterdam, 1402 p
- 636 Saxby J, Beckett F, Cashman K, et al. (2018) The impact of particle shape on fall velocity:
637 Implications for volcanic ash dispersion modelling. *J Volcanol Geotherm Res* 362:32–48.
638 doi: 10.1016/j.jvolgeores.2018.08.006
- 639 Scarlato P, Mollo S, Bello E Del, et al. (2016) The 2013 eruption of Chaparrastique volcano (El
640 Salvador): Effects of magma storage, mixing, and decompression. *Chem Geol* 448:110–
641 122. doi: 10.1016/j.chemgeo.2016.11.015
- 642 Schumacher R, Schmincke H (1991) Internal structure and occurrence of accretionary lapilli -
643 a case study at Laacher See Volcano. *Bull Volcanol* 53:612–634
- 644 Steffke AM, Fee D, Garces M, Harris A (2010) Eruption chronologies , plume heights and
645 eruption styles at Tungurahua Volcano : Integrating remote sensing techniques and
646 infrasound. *J Volcanol Geotherm Res* 193:143–160. doi:
647 10.1016/j.jvolgeores.2010.03.004
- 648 Stinton AJ, Cole PD, Stewart RC, et al. (2014) The 11 February 2010 partial dome collapse at
649 Soufriere Hills Volcano, Montserrat. *Geol Soc London, Mem.* 39(1), 133–152. doi:
650 10.1144/M39.7
- 651 Stumm W, Morgan JJ (1996) Aquatic Chemistry: Chemical Equilibria and Rates in Natural
652 Waters. John Wiley & Sons.
- 653 Taddeucci J, Scarlato P, Montanaro C, et al. (2011) Aggregation-dominated ash settling from
654 the Eyjafjallajökull volcanic cloud illuminated by field and laboratory high-speed
655 imaging. *Geology* 39:891–894. doi: 10.1130/G32016.1
- 656 Taylor PS, Stoiber RE (1973) Soluble Material on Ash from Active Central American
657 Volcanoes. *Geol Soc Am Bull* 84:1031–1042
- 658 Van Eaton AR, Muirhead JD, Wilson CJN, et al. (2012) Growth of volcanic ash aggregates in
659 the presence of liquid water and ice: an experimental approach. *Bull Volcanol* 74:1963–
660 1984. doi: 10.1007/s00445-012-0634-9
- 661 Witham CS, Oppenheimer C, Horwell CJ (2005) Volcanic ash-leachates: A review and
662 recommendations for sampling methods. *J Volcanol Geotherm Res* 141:299–326. doi:
663 10.1016/j.jvolgeores.2004.11.010

664 Wright HMN, Cashman K V, Mothes PA, et al (2012) Estimating rates of decompression from
665 textures of erupted ash particles produced by 1999 – 2006 eruptions of Tungurahua
666 volcano , Ecuador. *Geology* 40:619–622. doi: 10.1130/G32948.1

667

668 **Tables and figure captions**

669

670 **Table1.** Results from the leaching analysis showing the concentrations of anions and single
671 elements in ppm.

672

673 **Figure 1.** Concentrations in ppm of Na, Cl⁻, Ca, SO₄²⁻, K and Mg in aggregates from Hunga
674 Tonga-Hunga Ha'apai, Soufrière Hills, Tungurahua and Chaparrastique. For Hunga Tonga-
675 Hunga Ha'apai, a range is given for each ion. The dashed blue line corresponds to the highest
676 Cl⁻ content previously found in the literature in ash samples from Irazú volcano, Costa Rica
677 (Taylor and Stoiber, 1973). The grey field corresponds to the range for the highest SO₄²⁻
678 concentrations found at Ruapehu (Cronin et al., 2003) and Kilauea (Damby et al., 2018).

679

680 **Figure 2.** SEM BSE images and chemical mapping revealing the presence of NaCl and CaSO₄
681 in the ash rims of lapilli from sample HH33. a to e: Large CaSO₄ salt (in blue) and Cl bearing
682 salts visible in the Cl elemental map in (e). f to i: Large NaCl salt (in green) and smaller CaSO₄
683 salts (in blue).

684

685 **Figure 3.** Correlations between the molar concentrations of Na-Cl and Ca-SO₄ revealing an
686 approximately 1:1 relationship implying the presence of salts NaCl and CaSO₄ in the ash rims
687 prior to leaching.

688

689 **Figure 4.** Evolution of the saturation state of seawater with respect to carbonate, sulfate and
690 chloride salts during evaporation. The amount of different salts as a function of the
691 concentration factor (a) and the degree of evaporation (b) are shown.

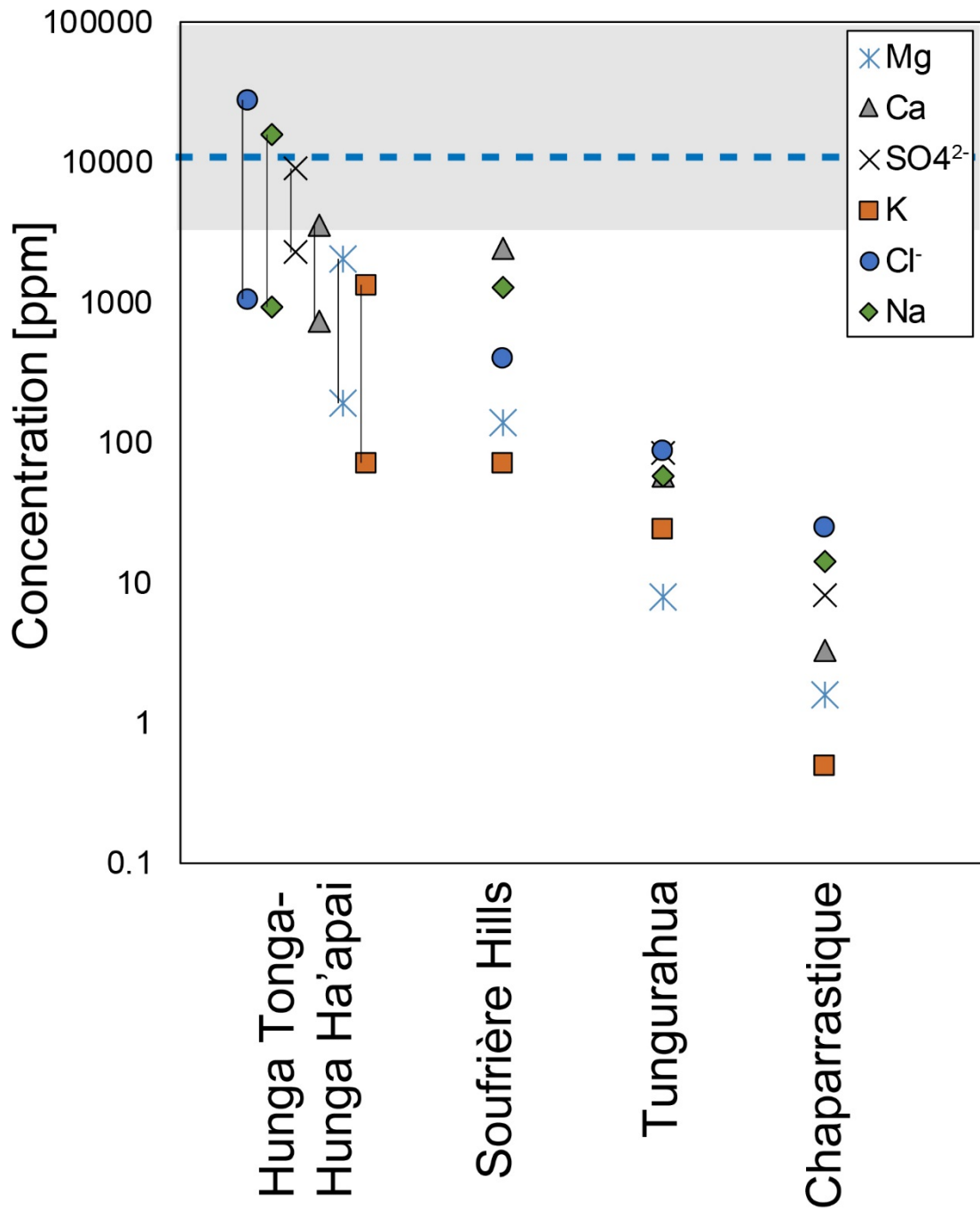
692

693 **Figure 5.** Evolution of concentrations in Cl⁻, Na, Ca and SO₄²⁻ analyzed in the aggregates from
694 Hunga Tonga-Hunga Ha'apai as a function of their position in the stratigraphic sequence of the
695 cone-building phase.

696

697 **Figure 6.** Schematic representation of the spectrum of natural volcanic settings for salt
 698 precipitation considered in our study and expected salt concentrations. Subaerial eruptions with
 699 massive degassing, presence of a crater lake and hydrothermal activity are not shown in this
 700 diagram but also represent natural settings with extensive salt formation.

701

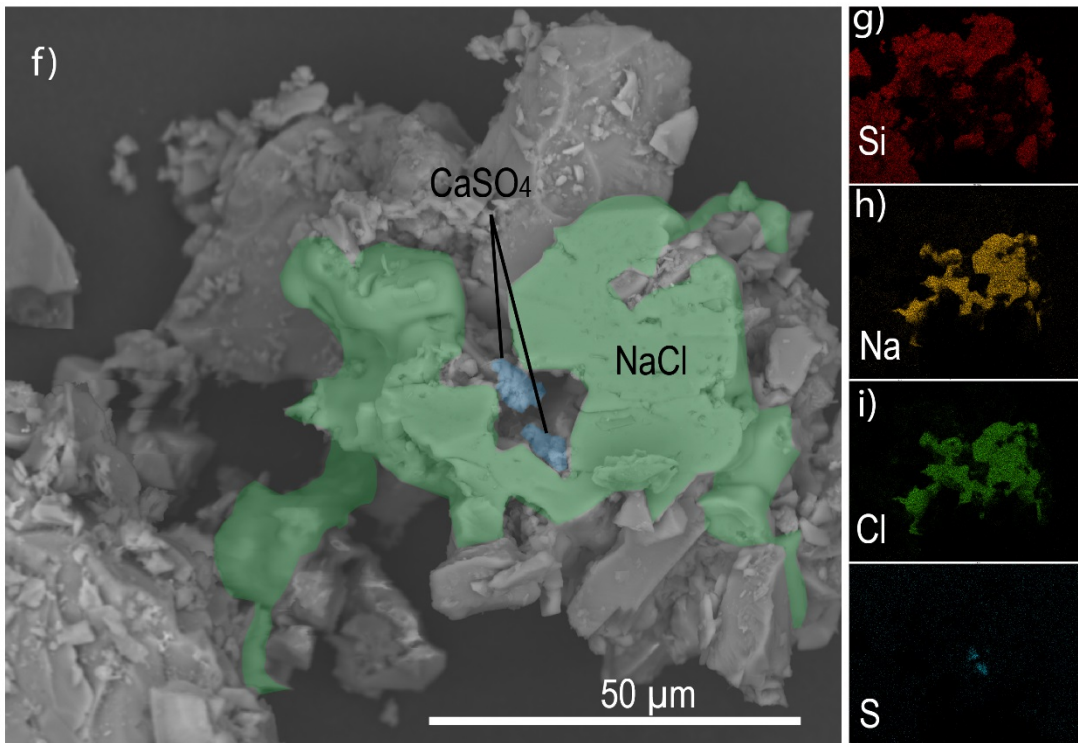
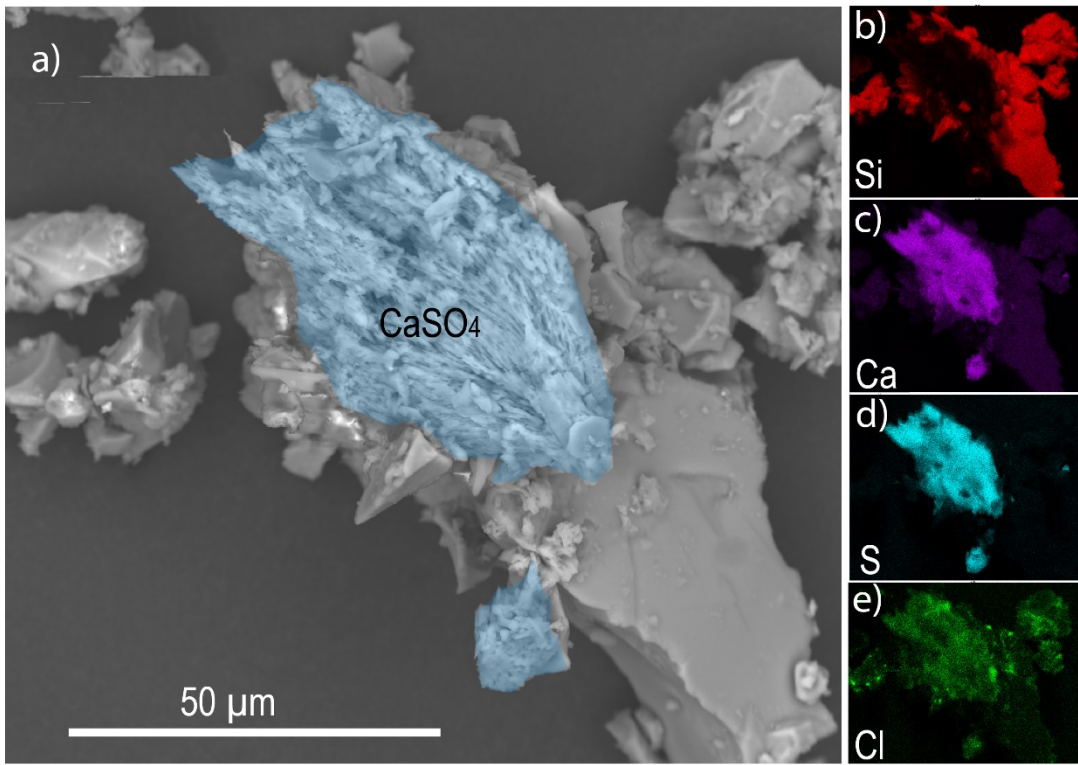


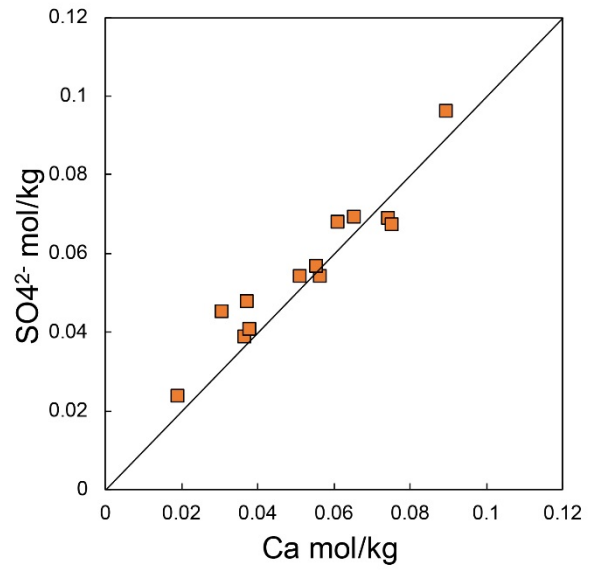
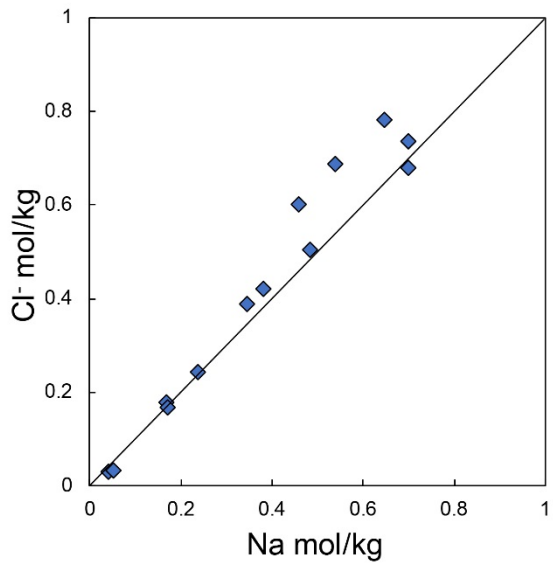
702

703

704

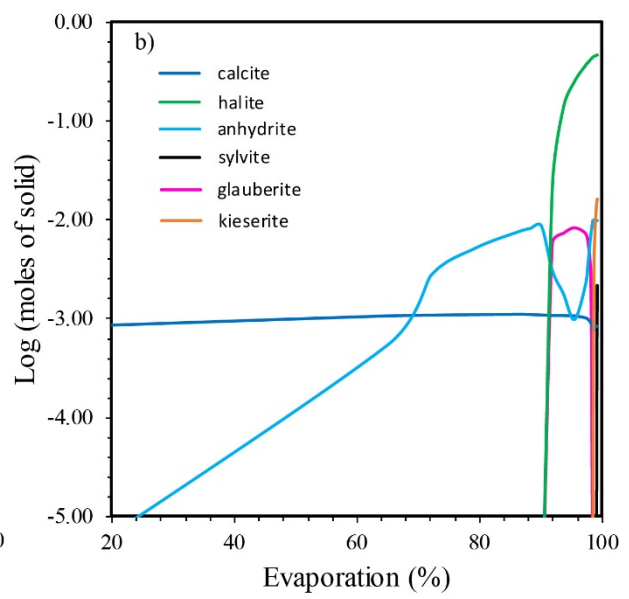
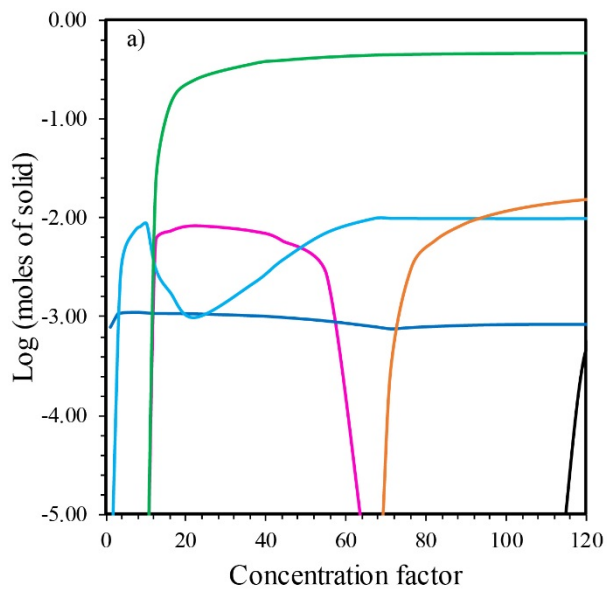
705





710

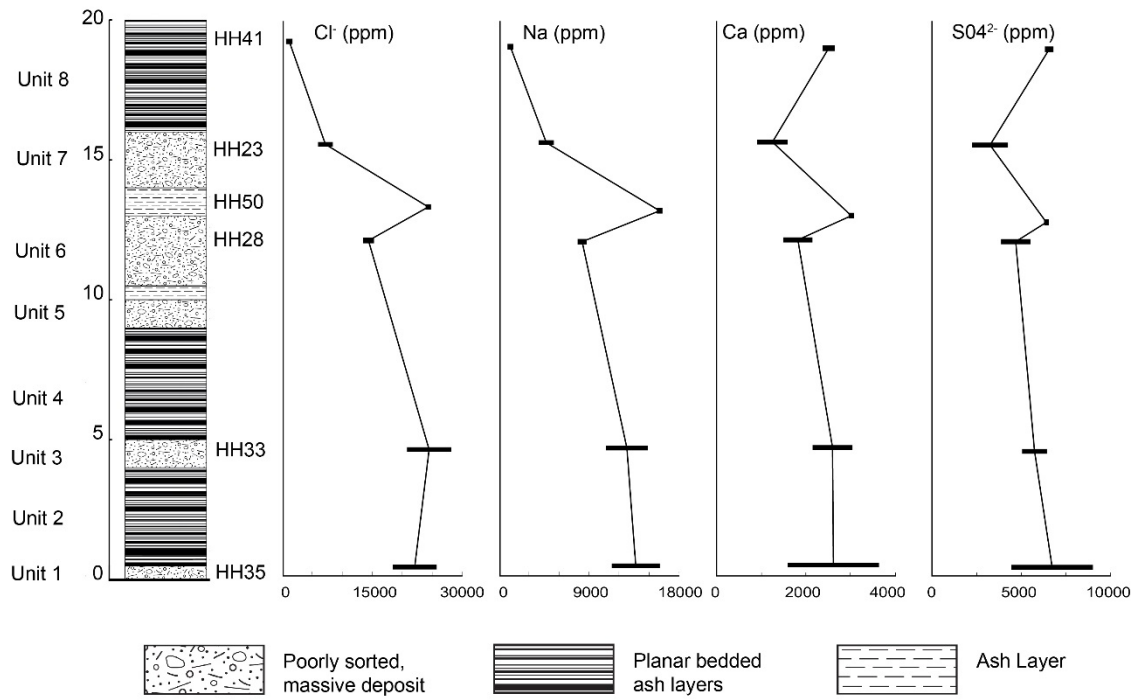
711



712

713

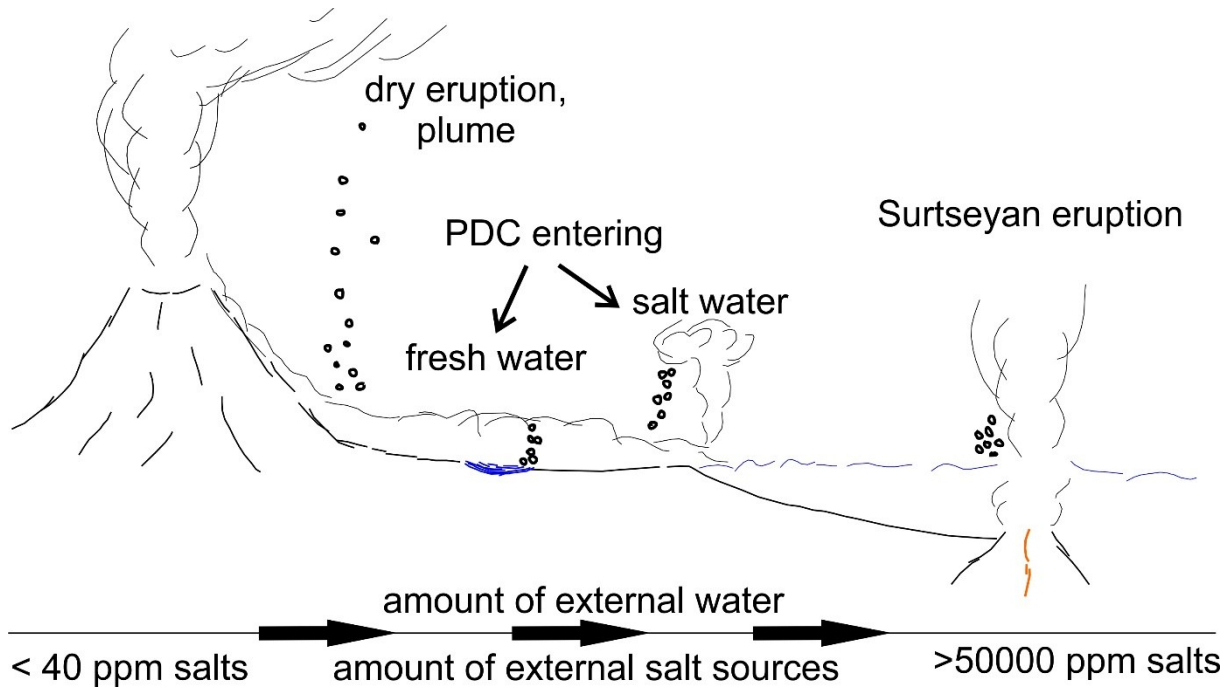
714



715

716

717



718

719

720

Study	Volcano	Type	Dilution ratio	Sample	Si	Mg	Ca	Na	K [ppm]	Mn	Cl ⁻	SO ₄ ²⁻
This study	Hunga Tonga- Hunga Ha'apai, Tonga	aggregates	1:100	23	725	321	753	3828	164	14	6325	2291
	Hunga Tonga- Hunga Ha'apai, Tonga	aggregates	1:500	23	3551	351	1451	5420	164	17	8605	3733
	Hunga Tonga- Hunga Ha'apai, Tonga	aggregates	1:1000	23	7255	323	1215	3939	153	17	5879	4344
	Hunga Tonga- Hunga Ha'apai, Tonga	aggregates	1:500	41	-	194	2425	932	72	-	1060	6511
	Hunga Tonga- Hunga Ha'apai, Tonga	aggregates	1:1000	41	-	210	2600	1188	78	-	1182	6650
	Hunga Tonga- Hunga Ha'apai, Tonga	aggregates	1:500	50	-	1727	3000	16070	1325	-	24099	6450
	Hunga Tonga- Hunga Ha'apai, Tonga	aggregates	1:100	33	1597	1817	2034	14850	530	53	27703	5200
	Hunga Tonga- Hunga Ha'apai, Tonga	aggregates	1:500	33	7740	1940	2249	10555	589	60	21270	5202
	Hunga Tonga- Hunga Ha'apai, Tonga	aggregates	1:1000	33	14900	2049	2956	12350	593	73	24332	6601
	Hunga Tonga- Hunga Ha'apai, Tonga	aggregates	1:1000	35	7185	1201	3563	16060	436	25	26082	9230
	Hunga Tonga- Hunga Ha'apai, Tonga	aggregates	1:1000	35	7308	657	1485	11070	242	16	17814	4599
	Hunga Tonga- Hunga Ha'apai, Tonga	aggregates	1:500	28	-	676	1500	7920	239	-	13732	3919
	Hunga Tonga- Hunga Ha'apai, Tonga	aggregates	1:1000	28	-	768	2200	8725	303	-	14902	5455
	Soufrière Hills, Montserrat	aggregates	1:500	-	-	140	2462	1297	72	-	400	-
	Tungurahua, Ecuador	aggregates	1:500	-	-	8	58	58	24	-	88	85
Chaparrastique, El Salvador	aggregates	1:500	-	-	2	3	14	1	-	25	8	
Soufrière Hills, Montserrat	non-aggregated material	1:500	-	-	31	1395	218	14	-	85	-	
Tungurahua, Ecuador	non-aggregated material	1:500	-	-	4	40	37	11	-	49	86	
Whitham et al., 2005	Compilation	-	-	-	-	-	-	-	-	4-11160	2-21775	
Ayris and Delmelle, 2012	Compilation	-	-	-	<1-4240	<1-23590	<1-2560	<1-788	<1-144	-	-	
Cronin et al., 2003	Ruapehu	seawater concentrations	-	-	1272	400	10561	380	0.01	18980	2712	

721